Advanced Nickel-based Catalytic Materials on Hydroxyapatite: Effect of the Metal Particle Size on Tri-reforming of Methane

Alejandro Perez Alonso, Alejandro Serrano-Maldonado, Jean-Bernard Ledeuil, Lénaïc Madec, Doan Pham Minh, Daniel Pla, Montserrat Gómez

https://doi.org/10.1021/acssusresmgt.3c00099

Advanced Nickel-based Catalytic Materials on Hydroxyapatite: Effect of the Metal Particle Size on Tri-reforming of Methane

Alejandro Pérez Alonso,[a] *Alejandro Serrano-Maldonado,*[a] *Jean-Bernard Ledeuil,*[b] *Lénaïc Madec,*[b] *Doan Pham Minh,*[c*] *Daniel Pla,*[a*] *Montserrat Gómez,*[a*].

[a] Laboratoire Hétérochimie Fondamentale et Appliquée, UMR CNRS 5069, Université Toulouse 3 – Paul Sabatier, 118 route de Narbonne, 31062 Toulouse Cedex 9, France.

[b] Institut des Sciences Analytiques et de Physicochimie pour l'Environnement et les Matériaux, Université de Pau et des Pays de l'Adour, UMR CNRS 5254, 2 avenue du président Angot, 64053 Pau, France.

[c] Centre RAPSODEE, IMT Mines Albi, UMR CNRS 5302, Université de Toulouse, Campus Jarlard, 81013 Albi Cedex 9, France.

ABSTRACT

A new strategy based on an organometallic approach for the preparation of Ni-based catalytic materials permitting to control the morphology and distribution of the nanoparticles on the support has been developed, leading to spherical, small (mean diameter below 5 nm) and homogenously distributed nickel nanoparticles on hydroxyapatite. The as-prepared materials were characterized by different techniques (N_2-physisorption, powder X-ray diffraction, transmission electron microscopy, infrared spectroscopy, temperature programmed reduction, temperature-programmed desorption of ammonia, temperature-programmed desorption of carbon dioxide and thermogravimetric analyses, among the most relevant). The catalytic performance of

these materials was evaluated in the tri-reforming of methane at 800-850 ºC and 1.4 bar (molar feed composition CH_4:CO_2:H_2O:O_2 = 63.3:30.7:0.04:5.95, gas hourly space velocity = 14.9 $L \cdot g_{cat}^{-1} \cdot h^{-1}$), in view of syngas production. Outstanding catalytic performance, in terms of activity, selectivity and stability, were achieved with the catalysts prepared via an organometallic method precluding structural modifications on the support. A comparative study between these catalytic materials proved higher activity and stability of the aforementioned materials in comparison with those prepared by a conventional incipient wetness impregnation methodology, mainly associated to stronger metal support interactions and higher surface area.

1. Introduction

Synthetic gas or syngas is an important platform gas mixture in chemical industry. To-date, syngas is mainly produced by gasification of coal, petroleum, petcoke, biomass and wastes (42% in 2017), and by steam methane reforming (SMR; 58% in 2017).[1] At industrial scale, SMR is usually performed over a nickel-based catalyst, at high temperature (ca. 900 °C), high pressure (10-20 bar), and high molar steam-to-carbon ratio (S/C of 3-4, which is the feed molar ratio of H_2O to CH_4).[2] High S/C ratio is used not only to maximize methane conversion, but also to prevent catalyst deactivation by coke deposition.[3] However, since the downstream uses of syngas usually require much lower temperatures (e.g. Fisher-Tropsch synthesis operating at 220-350 °C,[4] methanol synthesis at temperatures ranging from 90-350 °C,[5] or water-gas shift reaction at 200-450 °C),[6] the syngas generated from SMR units should be cooled down, requiring heat exchangers, which usually engender considerable heat loss. As recently reported, among the different alternative solutions to SMR, tri-reforming of methane (TRM) appears as the best option for syngas production from methane (eq. 1).[7, 8] In fact, TRM combines steam methane reforming (SMR), partial oxidation of methane (POM) and dry methane reforming (DMR) in a unique process that converts a mixture of methane, steam, oxygen and carbon dioxide into syngas (eqs. 2-4). Thus, the H_2/CO molar ratio of the resulting syngas can be controlled by changing feed composition, which is important for further downstream applications. Moreover, TRM can also

be performed with molar ratios of $(H_2O + O_2 + CO_2)/CH_4$ close to stoichiometry at relatively moderate temperatures (750-800 °C), while precluding coke formation which is a major advantage of TRM in comparison with other methane reforming processes.

$$x\ CH_4 + y\ CO_2 + z\ H_2O + t\ O_2 \rightarrow a\ CO + b\ H_2 \quad \textit{Trireforming of Methane} \quad \text{(eq. 1)}$$

$$CH_4 + H_2O \rightarrow 3\ H_2 + CO \quad \textit{Steam Reforming of Methane} \quad \text{(eq. 2)}$$

$$CH_4 + 1/2\ O_2 \rightarrow 2\ H_2 + CO \quad \textit{Partial Oxidation of Methane} \quad \text{(eq. 3)}$$

$$CH_4 + CO_2 \rightarrow 2\ H_2 + 2\ CO \quad \textit{Dry Reforming of Methane} \quad \text{(eq. 4)}$$

As recently reviewed by Pham *et al.*,[7, 8] nickel-based catalysts are the most studied in TRM. However, the achievement of outstanding TRM catalysts, exhibiting high activity and high stability profiles is actively sought, taking into account the complexity of TRM reaction encompassing a set of parallel processes.[7, 8] Several factors can impact the performance of a TRM catalyst, such as the arrangement and dispersion of active sites, the metal-support interaction (MSI), the catalyst loading, the reducibility of active phase, the sensibility to oxygen, and the thermal stability. Among them, downsizing nickel nanoparticle size highly favors the performance of TRM catalysts.[9] In the literature, nickel-based catalysts are usually prepared by the classical impregnation method, which is easy to perform at low cost and low waste generation. However, this approach generally leads to the formation of large nickel particles of dozens to hundreds nanometers.[10] Other preparation methods such as microemulsion,[11] hydrothermal,[12] solvothermal,[13] or templating effects[14] enable the formation of smaller nickel particle size by modifying several synthesis parameters such as the pH, temperature, ageing time, and metal-support interactions. However, the nickel particle sizes reported in the literature are still large, *ca.* in the range of 6-16 nm (see Table S1 in the Supporting Information). Among them, Kumar's group reported the preparation of Ni-Cu alloy featuring a mean metallic particle size of 6.5 nm.[15] The preparation of this catalyst needed an extra doping agent in order to reduce metallic particle size, that resulted in a performance enhancement towards TRM reaction.[15] Kumar's group also

highlighted the importance of both, the nature of the support and the preparation conditions, in the activity of the as-prepared catalysts.

The design of nickel nanocatalysts exhibiting high surface areas and enhanced reactivity profiles arising from low-coordination sites due to structural defects,[16] and synergistic effects between metal-support interfaces,[17] represents an innovative strategy towards the kinetic stabilization of small nanoparticles that has been widely applied by our group for zero-valent Ni systems immobilized both in a liquid phase (glycerol)[18] and solid supports ($MgAl_2O_4$,[19] TiO_2,[19] halloysite).[20]

In the quest towards well-defined catalysts nanocomposites, we surveyed the nature of catalyst supports taking into account its crucial role in the catalytic performance of a reforming catalyst. For TRM reaction, standard catalyst supports such as silica, ceria, titania, magnesia alumina and lanthanum oxide have been investigated.[7] Furthermore, alternative supports such as hydroxyapatite [HAP, $Ca_{10}(PO_4)_6(OH)_2$] featuring a high density of basic sites have also been reported in the literature in combination with Ni and Rh, furnishing promising catalytic materials for SMR,[21] POM,[21] and DMR.[22] Hitherto, Jun et *al*.[23] have reported the smallest nickel particle sizes comprised within the range of 5-20 nm on HAP, albeit particle dispersion was not optimized.

The present work focuses on the development of small nickel nanoparticles (NiNPs) immobilized on a HAP support by using novel synthetic methodologies in combination to characterization techniques towards TRM catalyst assessment. To the best of our knowledge, TRM catalysts featuring smaller than 5 nm nanoparticles have, thus far, never been reported.

2. Experimental section

2.1. Synthesis of HAP-supported nickel catalysts with and without stabilizer (quinidine).

A Fisher-Porter bottle was charged with bis(cyclooctadiene)nickel(0) (343.0 mg, 1.25 mmol for 5 wt.%; 646 mg, 2.5 mmol for 10 wt.% Ni), HAP (1497 mg, 5.09 mmol) and in the case of the presence of a stabilizer with quinidine (371.0 mg, 1.15 mmol), and then sealed with a

septum inside the glovebox. The Fisher-Porter bottle was then removed from the glovebox and the solids were suspended in degassed EtOH (50 mL) under Ar prior to sealing the Fisher-Porter with its head. The system was then pressurized with H_2 (3 bar) at room temperature, and then heated to 100 °C under stirring for 18 h. The black suspension formed was transferred to a centrifuge tube under Ar, which was then centrifuged at 3000 rpm for 5 min. The solid was recovered and washed three times with degassed EtOH. The resulting black solid was dried under vacuum overnight and stored in the glovebox prior to use. Four materials containing 5 and 10 wt.% nickel loadings were prepared in the absence (denoted as **5Ni@HAP** and **10Ni@HAP**) and in the presence of quinidine (**5Ni-QD@HAP** and **10Ni-QD@HAP**) (see Scheme 1, as well as Schemes S1-S3 and Figures S1-S3 in the Supporting Information). For the synthesis of HAP-supported nickel catalysts by incipient wetness impregnation methodology, see section 2.5 in the Supporting Information.

2.2. Ni-catalyzed TRM reaction

TRM reactions were carried out in a tubular fixed-bed ceramic reactor (8 mm inner diameter, 25 cm length) (see Figure S6 in the Supporting Information). A thermocouple was set at the center of catalyst bed to control the reaction temperature. For a given test, the reactor was firstly filled with inert alumina powder (previously treated at 1000 °C in air; specific surface area of 3 $m^2 \cdot g^{-1}$). Then, 340 mg of HAP supported Ni catalyst were mixed with 340 mg of alumina and placed at the center of the fixed-bed reactor. The reactor was then filled with an additional layer of alumina. Prior to the TRM reaction, the catalyst was reduced *in-situ* at 700 °C for 2 h under 4 vol% H_2/N_2 (70 NmL min^{-1}) with the aim of reducing plausible nickel oxide species. The reactor was then heated to the desired reaction temperature (800 °C or 850 °C), prior to feeding the reactor with a mixture of $CH_4/CO_2/H_2O/O_2$ = 63.3/30.7/0.04/30.65 (vol.%, 75 NmL min^{-1} total gas flow rate). The inlet flow of each of the gases and water was individually calculated after passing through the reactor without any type of catalyst or other reagent: CH_4 47.5 mL/min, CO_2

23.0 mL/min, O_2 4.5 mL/min and H_2O 0.03 mL/min; then, for each gas the volume percentage was calculated. Under these conditions, the pressure drop inside the reactor was *ca.* 0.4 bar leading to a total pressure equal to 1.4 bar, which was monitored by a pressure sensor inside the reactor. Unconsumed water was quantified by a water trap, composed of a silica gel tube, which was periodically weighed during the reaction. The total flow rate of the dried outlet gas was measured by a gas counter, while its composition was analyzed with a μ-GC.

For the determination of conversion, selectivity, NiNPs dispersion and total turnover frequency, see section 3 in the Supporting Information.

3. RESULTS

3.1. Synthesis of the Ni-based catalytic materials

Ni-based materials were prepared through a one-pot organometallic methodology based on our previously reported works.[19, 20, 24, 25] Thus, *in-situ* decomposition of bis(1,5-cyclooctadiene)nickel(0) was carried out under hydrogen (3 bar), in the presence of hydroxyapatite (HAP) as support and quinidine (QD) as stabilizer (molar ratio Ni:support:stabilizer = 1:4.1:0.9) at 100 °C in ethanol during 18 h (**xNi-QD@HAP**, where x = 5 and 10, meaning the expected weight percentage of nickel on the catalytic material; Scheme 1), obtaining a black dispersion. The main parameters were optimized (metal loading, pressure and reaction time; see Supplementary Information). For each approach (in the presence and in the absence of quinidine), ICP-AES analyses proved that no nickel leaching occurred during the workup (Table 1).

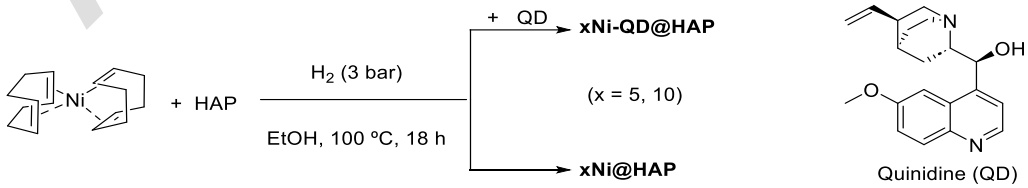

Scheme 1. One-pot organometallic approach for the synthesis of NiNPs supported on HAP (x meaning the expected weight percentage of nickel present on the catalytic material).

Moreover, we prepared NiNPs supported on HAP by a sequential organometallic decomposition methodology (for experimental details, see Supporting Information). Thus, NiNPs were firstly prepared in glycerol using [Ni(cod)$_2$] as metallic precursor and quinidine as stabilizer, based on our previous reported works.[18] After isolation of the nanoparticles by centrifugation (showing a mean diameter of ca. 2 nm), the resulting NiNPs were immobilized on HAP. ICP-AES analysis of the as-prepared material indicated that only *ca*. 20% of the initial nickel content was immobilized by this method, evidencing the inaptness of this approach.

For comparative purposes, Ni-based catalytic materials were prepared by incipient wetness impregnation method (IWI), the most widely applied synthetic approach for heterogeneous catalytic materials, due to its simplicity, avoiding the formation of wastes (see Scheme S4 in the Supporting Information),[7] leading to materials **xNi@HAP_IWI** (x = 5 and 10, meaning the expected weight percentage of nickel on the catalytic material).

3.2. Characterization of the prepared Ni-based catalytic materials

Ni content obtained by ICP-AES analysis for the different materials was close to the expected value (5 wt.% or 10 wt.%, depending on the starting amount of nickel precursor), validating the high efficiency of the one-pot organometallic immobilization method in comparison with the IWI procedure (Table 1). The preparation method has a dramatic impact in the nickel dispersion. For the materials prepared via the organometallic approach, dispersions are up to ten times higher than those obtained for IWI, in agreement with the smaller Ni particle sizes (Table 1).

Table 1. Metal content, specific surface area, mean diameter of NiNPs and Ni dispersion on hydroxyapatite of the as-prepared catalytic materials.

Catalytic material	Ni loading (wt.%)[a]	Surface area	Mean diameter of NiNPs (nm)[c]	Ni dispersion (%)[d]

		$(m^2 \cdot g^{-1})^b$		
HAP support	-	60 ± 1.4	-	-
5Ni-QD@HAP	4.6 ± 0.0	56 ± 0.7	2.6 ± 1.6	38.1
10Ni-QD@HAP	9.5 ± 0.1	118 ± 1.4	3.8 ± 1.9	26.6
5Ni@HAP	4.7 ± 0.2	54 ± 0.7	2.8 ± 1.8	36.0
10Ni@HAP	10.1 ± 0.2	120 ± 2.1	4.4 ± 1.8	22.9
5Ni@HAP_IWI	5.1 ± 0.3	42 ± 0.7	38.0 ± 26.0	2.6
10Ni@HAP_IWI	9.7 ± 0.2	37 ± 0.7	27.0 ± 18.0	3.1

[a] Determined by ICP-AES. [b] Determined according to BET theory. [c] Calculated from TEM images after extraction of NiNPs with glycerol. [d] See Supplementary Information for definition and calculation.

The textural properties of the support and fresh calcined catalytic materials were determined through nitrogen adsorption-desorption isotherm analyses (see Figure S7 in the Supporting Information). The as-prepared materials followed an isotherm of type II, according to the classification of IUPAC,[26] with gradual curvature (indistinguishable knee) indicating a monolayer coverage and the beginning of a multilayer absorption. These materials showed hysteresis of H3 type, characteristic of materials with a leaf-shaped structure.

The catalysts prepared by the organometallic synthesis route containing a high metal loading (ca. 10 wt.% Ni) showed a higher specific surface area (118 and 120 m^2/g respectively for **10Ni-QD@HAP** and **10Ni@HAP**) in comparison with that of the pristine support (60 m^2/g). This behavior might be due to the modification of the support surface by fixation of small Ni nanoparticles (< 5 nm, see below TEM analysis discussion) at relatively high metal loadings (10 wt.%), as previously reported for surface modification of graphene oxide composites with NiNPs[27] and Pt-loaded[28] on TiO_2 nanoparticles. However, the specific surface area determined by

BET analyses for **5Ni-QD@HAP** and **5Ni@HAP** were close to the values exhibited by the support (56 and 54 m^2/g respectively). Instead, the catalytic materials prepared by the conventional IWI method showed a smaller specific surface area than that corresponding to neat HAP (**5Ni@HAP_IWI** and **10Ni@HAP_IWI**, 42 and 37 m^2/g respectively). As later evidenced by TEM analysis, the catalysts prepared by IWI contain large Ni particles, which can potentially clog the pores of HAP support, consequently reducing the specific surface area.

The as-prepared materials were characterized by TEM with the aim of observing the morphology of NiNPs (size, shape) and their distribution on the support. The TEM images of **5Ni@HAP_IWI** and **10Ni@HAP_IWI**, both prepared by the conventional impregnation methodology, showed the formation of large particles non-homogeneous in size and agglomerates (see Figure S5 in the Supporting Information). For all the materials prepared by the organometallic approach, the direct observation of metal nanoparticles was not possible probably due to their small size (see Figure S8 in the Supporting Information). With the purpose of extracting the nanoparticles immobilized on the support and thus determining their mean size, we dispersed the catalytic materials in glycerol taking advantage of the high affinity of metal nanoparticles by this solvent as proven previously by our group.[19] Actually, we could extract more than 80% of nickel from the solid materials as evidenced by ICP-AES for the catalytic materials prepared by the organometallic procedure; for those prepared by IWI method, the glycerol extraction was not efficient due to the low affinity of the large particles formed for a polar solvent such as glycerol (see Table S2 in the Supporting Information). Given the negligible vapor pressure of glycerol, TEM analyses showed the formation of spherical nanoparticles of mean diameters in the range of 2.6 – 4.4 nm (Table 1 and Figure 1), being smaller for those materials containing lower nickel loading, *e.g.* **5Ni-QD@HAP** and **5Ni@HAP**. This demonstrates the advantage of the organometallic synthesis approach to downsize the nickel nanoparticles, in comparison with conventional incipient wetness impregnation methods.

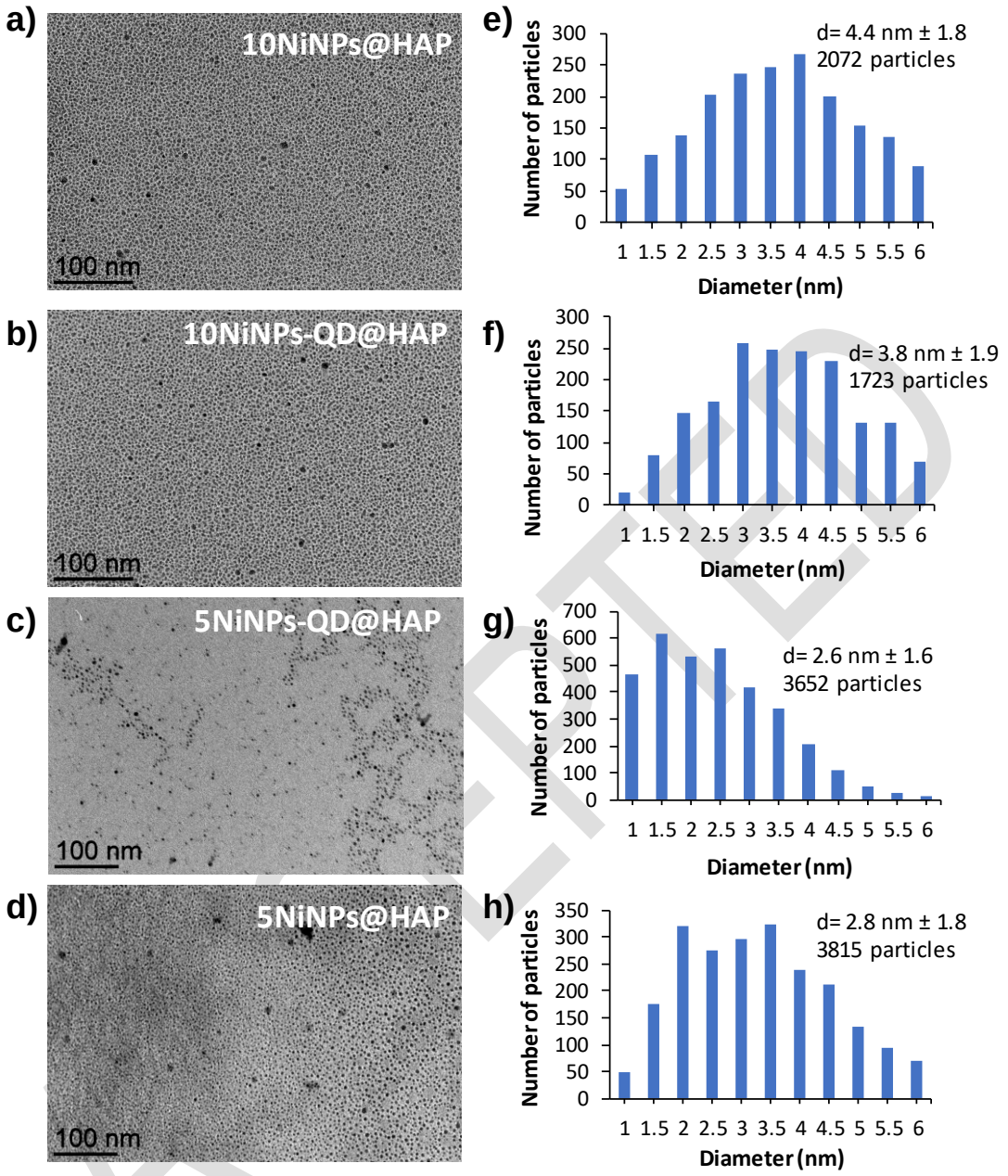

Figure 1. TEM images (a-d) and the corresponding size histograms (e-h) of the Ni-based materials prepared by the organometallic approach after extraction with glycerol from the solid materials: a, e) **10Ni-QD@HAP**; b, f) **10Ni@HAP**; c, g) **5Ni-QD@HAP**; and d, h) **5Ni@HAP**.

Taking into account that the thermal pre-treatment applied to the as-prepared catalytic materials in the TRM reactor before adding the gas mixture (CH_4, CO_2, O_2, H_2O; see above section

2.2), the **10Ni@HAP** catalyst (showing the best catalytic performance, see below section 3.3) was heated at 800 °C for 5 h followed by an extraction with glycerol. TEM analysis showed the presence of very small nanoparticles (mean size of 1.8 nm, see Figure S9 in the Supporting Information), smaller than before the thermal treatment (4.4 nm, Figure 1a and 1e); it is important to highlight that more than 80% of nickel could be extracted (checked by ICP-AES analyses: 8.4 wt.% before calcination and 1.4 wt.% after calcination). This behavior can be attributed to the formation of solid solutions between the support and nickel as previously observed by Kunzru and coworkers using NiNPs@$MgAl_2O_4$ in the steam reforming of methane.[29]

The as-prepared catalytic materials were analyzed by PXRD (see Figure S10 in the Supporting Information), exhibiting the characteristic peaks of the HAP support.[30] Unfortunately, the corresponding patterns to crystalline Ni phases (Ni(0), NiO) could not be identified, probably due to the small size of the nanoparticles or lack of crystallinity.[31]

FTIR spectra of the catalytic materials evidenced the presence of the functional groups of the HAP support (see Figure S11 in the Supporting Information). Regarding phosphate groups, peaks at 1087 and 1037 cm^{-1} were attributed to the asymmetric P-O stretching (v_1), the band at 960 cm^{-1} to the symmetric P-O stretching (v_3), and the bands at 601 and 561 cm^{-1} to P-O bending (v_4). The hydroxyls groups were characterized by the vibration bands at 634 cm^{-1}. Absorption bands corresponding to carbonate groups were not identified. Nitrate absorption bands were observed for catalytic materials prepared by IWI (region 1500-1300 cm^{-1}).

The thermal stability of the catalytic materials was determined by thermogravimetric analyses in air (TGA, Figure 2a). A small initial mass loss took place below 100 °C for the catalysts prepared by the organometallic strategy. This can be due to some residual ethanol and water physisorbed on hydroxyapatite even after the catalyst drying process. After this initial mass loss, all the samples behave in a similar way, exhibiting mass losses of 3.5-3.7% between 300 °C and 900 °C, in analogy to other HAP-based materials described in the literature.[32] All the as-prepared materials were thermally stable at the working temperature of TRM (800-850 °C, Figure

2a). Despite the reversible loss of hydroxyl groups in HAP has been described to take place in a large range of temperatures along the thermal treatment, TRM operating conditions in the presence of steam can help preserving the apatite structure via rehydration.[32]

The reducibility of the as-prepared catalytic materials was studied by temperature programmed reduction (TPR, Figure 2b). The catalysts prepared by the impregnation method showed similar behavior, observing a signal with two main peaks at 388 and 411 °C for 10 wt.% Ni loading (**10Ni@HAP_IWI**), and 381 and 402 °C for 5 wt.% Ni loading (**5Ni@HAP_IWI**) (see deconvolution analysis in Figure S12 in the supporting information); typical for NiO reduction slightly interacting with the support.[33] These catalysts showed higher H_2 uptake than the others, indicative of the higher content of nickel oxides.

For the catalytic materials prepared by organometallic approach, similar profiles were observed in those with the same Ni loading. The catalytic materials showed also similar TPR profiles between them. The deconvolution analysis of the signals profiles for **10Ni-QD@HAP** and **10Ni@HAP** (see deconvolution analysis in Figure S12 in the Supporting Information) revealed a small reduction peak at 421 °C for **10Ni-QD@HAP** and at 435 °C for **10Ni@HAP**, assigned to the reduction of α-type NiO species that have a weak interaction with the support.[34] A large peak around 485 °C was observed for both catalysts, indicative for a reduction of small particles of NiO with a stronger interaction with the support.[35] Moreover, a negative peak around 212 °C for **10Ni@HAP** was observed, probably due to decomposition of Ni-hydride species, considering the synthesis of catalytic materials was carried out under H_2.[34]

Nevertheless, the TPR profiles of the two catalysts with 5 wt.% Ni loading, were completely different from those with 10 wt.% Ni, exhibiting several large peaks between 245-600 °C and the lowest hydrogen uptake. For the deconvolution analysis of the **5Ni@HAP** profile **(**see Figure S12 in the Supporting Information), three peaks were observed. The first peak appears at 319 °C, indicative for NiO species with minimal or no interaction with the support.[36] The peaks

at 415 °C and 587 °C are characteristic for the reduction of α-NiO species with a weak interaction with the support, and β-NiO species with a stronger interaction with support, respectively.[34] In the case of **5Ni-QD@HAP**, three groups of peaks were observed. The first two peaks at 246 °C and 266 °C were assigned for partial reduction of NiO with no interaction with the support.[37] The next peaks at 345 °C and 413 °C were for the reduction of α-NiO species with a weak interaction with the support. Finally, a peak at 565 °C for the reduction β-NiO species with a stronger interaction with support, was observed.[34] The presence of free NiO species in these two catalysts is probably due to the smaller size of their NiNPs and consequently higher reactivity in TRM.

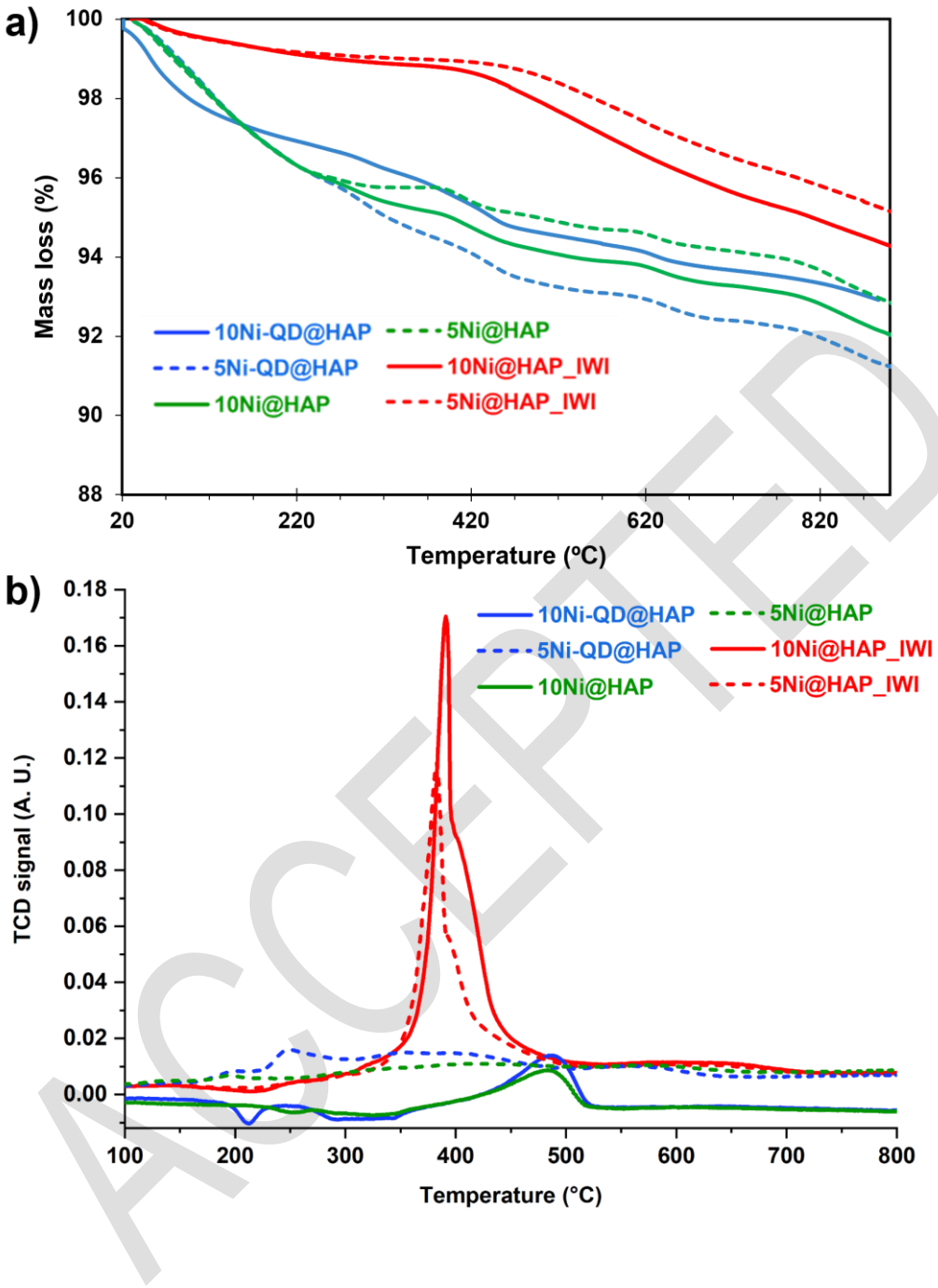

Figure 2. Thermogravimetric analysis (a) and temperature programmed reduction profiles (b) for the Ni-based catalytic materials supported on hydroxyapatite (for deconvolution treatment of TPR curves, see Figure S12 in the Supporting Information).

On the other hand, the TPR profiles of the two catalysts with 5 wt.% Ni loading, prepared by the same organometallic decomposition approach, were completely different from those of the

catalysts with 10 wt.% Ni loading. Actually, **5Ni@HAP** and **5Ni-QD@HAP** exhibited several large peaks between 200-600 °C, suggesting the formation of different nickel species on the surface of HAP with different metal-support interactions. The catalysts prepared by the impregnation method showed similar behavior, observing two main peaks at 397 and 404 °C for 10 wt.% Ni loading (**10Ni@HAP_IWI**) and 404 and 415 °C for 5 wt.% Ni loading (**5Ni@HAP_IWI**). These two reduction peaks are probably due to the multi-step reduction of nickel species, transforming Ni^{2+} to Ni^{x+} ($x < 2$), then Ni^{x+} to Ni(0), and also due to a moderate MSI, as suggested in the literature.[38] These analyses indicate that the catalytic materials prepared by the organometallic strategy exhibited stronger MSI compared to those prepared by impregnation.

CO_2-temperature-programmed desorption (CO_2-TPD) and NH_3-temperature-programmed desorption (NH_3-TPD) analyses were performed in order to evaluate the density of basic and acid sites respectively, and thus the activation of CO_2 during the reforming reactions (see Figure S13 in the Supporting Information). Only the catalysts containing 10 wt.% Ni, **10Ni@HAP**, **10Ni-QD@HAP** and **10Ni@HAP_IMP**, were characterized by these methods, due to their better catalytic performance (see the next section), together with the pristine HAP support. Regarding CO_2-TPD profiles (see Figure S13a in the Supporting Information), two peaks at *ca*. 120 °C and at 460 °C were observed for the pristine HAP support, suggesting the presence of basic sites (<500 °C), in agreement with the literature.[39] With respect to **10Ni@HAP_IWI**, a broad desorption peak appeared in the range *ca.* 690-750 °C, which is lower than the temperature used to conduct TRM process. Thus, precluding deleterious poisoning effect of CO_2 on the catalyst.

Regarding NH_3-TPD profiles, a large desorption peak between 90 °C and 460-510 °C for all the catalytic materials was observed similarly to the pristine support, suggesting the presence of acid sites with different strengths (see Figure S13b in the Supporting Information), taking into account the acid-base properties of apatite materials due to the presence of functional groups

(Ca^{2+}, PO_4^{3-}, HPO_4^{2-}). For the catalysts prepared by the organometallic approach, an increasing peak after 750 °C was observed due to the occurrence to desorption of ammonia from strong Lewis acid sites, in agreement with previously reported works.[40]

Considering the catalytic performance of **10Ni@HAP** (see below, section 3.3), X-ray photoelectron spectroscopy (XPS) analysis of this material was performed to identify the elements at the surface of the catalytic material and their oxidation states, in particular for the nickel nanoparticles immobilized on HAP (Figure 3). The XPS survey spectrum of **10Ni@HAP** showed the presence of Ni as well as Ca, O, and P coming from the HAP support, with a non-negligible amount of C, already present as an impurity in the HAP support. Importantly, the Ni 2p XPS core level spectrum of **10Ni@HAP** showed three contributions: Ni(0) (51%), NiO (31%) and $Ni(OH)_2$ (18%) (Figure 3b). These results highlight that the organometallic approach is efficient to obtain zero-valent NiNPs, albeit its partial oxidation given its prone oxidation from oxygen traces even under ultra-high vacuum during XPS analysis and manipulation under Ar atmosphere (glovebox), as observed in the characterization of NiNPs catalysts previously reported.[19, 20] Moreover, the observed Ca/P atomic ratio by ICP AES (1.8) corresponds to the pristine HAP, confirming that the structure of the support remained unaltered during the synthesis (see Table S3 and Figure S14 in the Supporting Information). The organometallic synthetic methodology precludes the formation of $Ni_3(PO_4)_2$[41] via the exchange of Ca(II) ions by Ni(II) in HAP as reported using incipient impregnation methods, avoiding structural changes known to weaken the support structure.[38]

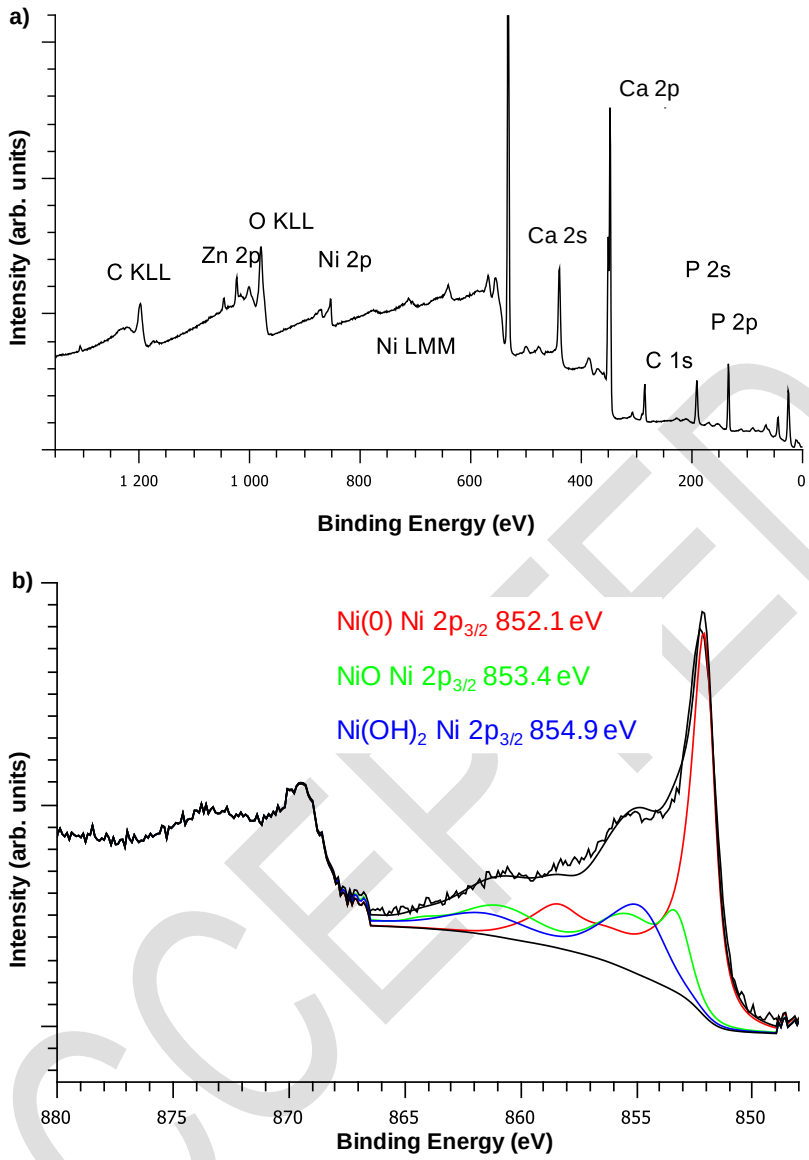

Figure 3. XPS analysis of **10Ni@HAP**: (a) XPS survey spectrum; (b) High-resolution spectrum at the binding region of Ni 2p. The fit was carried out on the Ni $2p_{3/2}$ binding energy by deconvolution considering the Ni(0) (red), NiO (green) and $Ni(OH)_2$ (blue) contributions; the black continuous trace corresponds to the sum of all of them.

3.3. Catalytic performance on TRM

We applied the as-prepared catalytic materials in the tri-reforming reaction of methane (eq. 1). The catalytic materials were activated prior to the reaction with a constant hydrogen flow

at 700 ºC; all the catalysts exhibited a reduction temperature below 600 ºC (see above TPR analyses). The reaction conditions (feedstock composition) were calculated to obtain a theoretical H_2/CO ratio of *ca.* 1.8, which is a suitable ratio for downstream hydroaminomethylation[42] and Fischer-Tropsch processes.[43] The performance of the catalysts was evaluated with regard to CH_4 and CO_2 conversions. In all cases, O_2 conversion was complete due to the high oxygen affinity for the active sites and the high oxygen reactivity for methane oxidation. For the determination of conversion, selectivity, NiNPs dispersion and total turnover frequency, see section 3 in the Supporting Information.

As expected, the catalysts with a higher nickel loading (10 wt.%) showed higher methane conversion than the corresponding catalysts prepared by the same method with a lower nickel loading (5 wt.%) (Figure 4). In this work, we monitored the reaction at long time (up to 70 h) only for the most active catalytic systems (it means, those constituted of 10 wt.% of nickel).

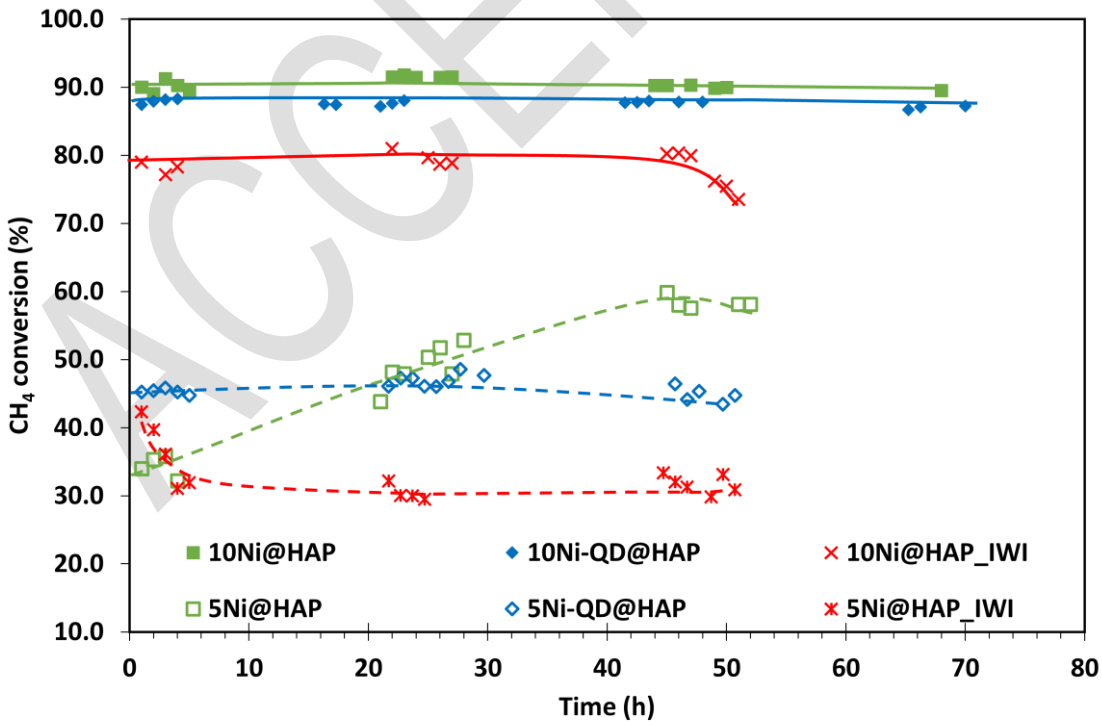

Figure 4. Methane conversions obtained with HAP-supported Ni catalysts. Reaction conditions: 800 °C, 1.4 bar (total pressure), $CH_4/CO_2/H_2O/O_2$ = 63.3:30.7:0.04:5.95 molar fraction. GHSV = 14.9 $L \cdot g_{cat}^{-1} \cdot h^{-1}$. Conversion determined by µ-GC.

The catalysts prepared by the organometallic approach with 10 wt.% Ni (**10Ni@HAP** and **10Ni-QD@HAP**, Figure 5) exhibited high initial conversions: 89-92% for CH_4 and 52-61% for CO_2 (Figure 5a and 5b respectively). Meanwhile, the catalyst prepared by impregnation method showed lower initial conversions (79% for CH_4 and 52% for CO_2). In terms of catalytic stability, **10Ni@HAP** and **10Ni-QD@HAP** showed nearly-constant CH_4 and CO_2 conversions during 72 h of time-on-stream (no deactivation observed). In contrast, **10Ni@HAP_IWI** showed initial catalytic stability (during the first 44 h of time-on-stream for methane conversion), prior to its deactivation. In addition, for this catalyst, the catalytic deactivation was particularly marked for CO_2 conversion. After 52 h of time-on-stream, the conversion dropped to 72% and 42% for CH_4 and CO_2 respectively. The feeding composition of the gas mixture corresponds to a quasi-stoichiometric molar ratio for the total conversion of methane by the three oxidants (steam, carbon dioxide and oxygen). The lower CO_2 conversion in comparison with that of CH_4 indicates that CO_2 is less active than O_2 and H_2O in the reforming of methane. The as-prepared catalysts via the organometallic approach exhibited higher catalytic performance in comparison with previously reported Ni-based catalysts for reforming processes (see Table S4 in the Supporting Information).

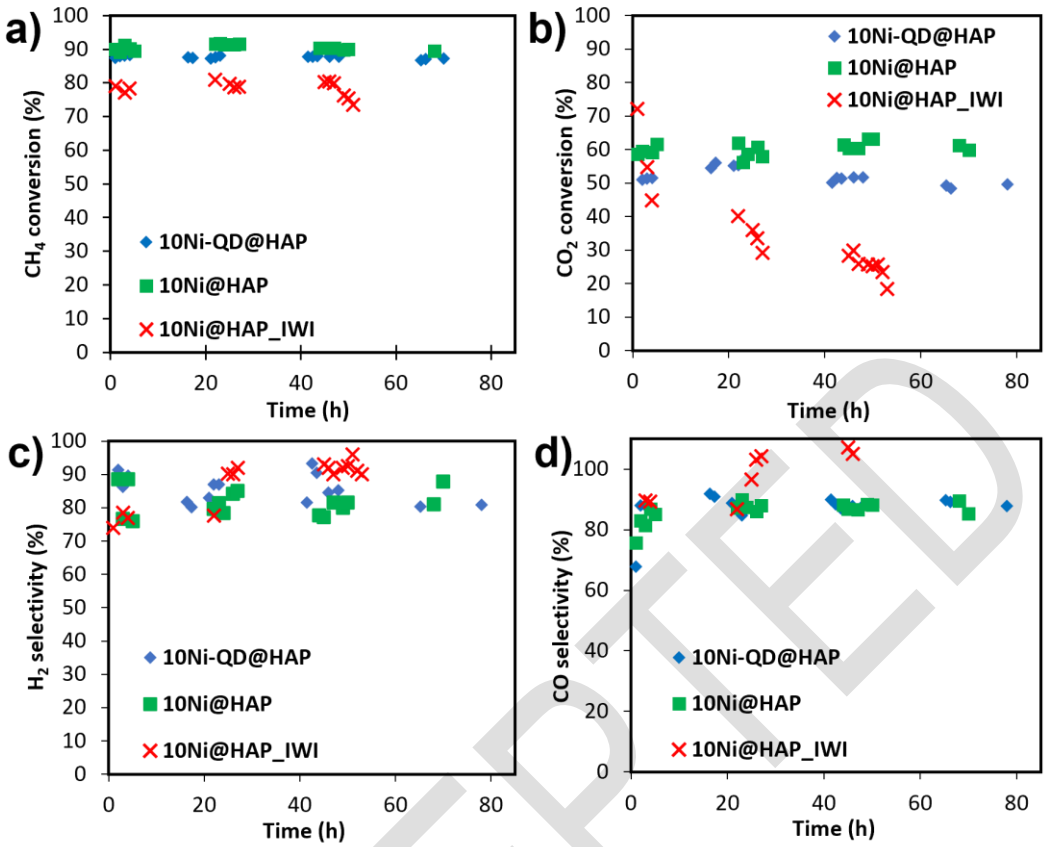

Figure 5. Catalytic performance of 10 wt.% Ni loading catalysts in the TRM reaction, **10Ni@HAP**, **10Ni-QD@HAP** and **10Ni@HAP_IWI**. Conditions: 800 °C, 1.4 bar (total pressure), $CH_4/CO_2/H_2O/O_2$ = 63.3:30.7:0.04:5.95 molar fraction: a) CH_4 conversion, b) CO_2 conversion, c) H_2 selectivity and d) CO selectivity. GHSV 14.9 = $L \cdot g_{cat}^{-1} \cdot h^{-1}$. Conversion and selectivity determined by µ-GC.

The selectivity of the catalysts for H_2 and CO was high (Figures 5c and 5d). In the case of **10Ni@HAP** and **10Ni-QD@HAP**, 87% for carbon monoxide and 83% for hydrogen was observed. It is interesting to highlight that the selectivity of **10Ni@HAP_IWI** was higher, being 92% for hydrogen and up to 100% for CO. Moreover, the decrease in the carbon dioxide conversion was directly proportional to the increase in the carbon monoxide selectivity. This behavior can be explained by the water-gas shift side reaction. The H_2/CO ratio remained

relatively constant over time, in particular for the catalysts prepared by the organometallic approach (see Figure S15 in the Supporting Information).

The H_2 selectivity of all the catalyst fluctuates along time. Nevertheless, for the catalysts prepared by IWI method, an increase in the H_2 selectivity was observed. This is due to side reactions (such as methane cracking, carbon gasification or water-gas shift reactions) which can gain importance while the reaction is ongoing. It is worth to mention that the stability exhibited by **10Ni@HAP** precluded H_2 fluctuations, in contrast to a selectivity decrease observed for **10Ni-QD@HAP**, probably due to concomitant reverse water-gas shift reaction or CO_2 methanation, the latter being highly unlikely, since the methane conversion remained constant all along the reaction and this reaction is preferentially takes place at lower temperature ranges.[44]

Regarding the CO selectivity, all the catalytic materials exhibited a similar selectivity (ca. 90%) with a high stability. Nevertheless, for **10Ni/HAP_IWI**, an increase in the carbon monoxide selectivity was observed. The coke formed at the surface together with CO_2 can probably lead to comproportionation, increasing the amount of CO.

Catalytic materials with 5 wt.% Ni loading exhibited a different catalytic behavior (see Figure S16 in the Supporting Information) in comparison with their 10 wt.% Ni counterparts (Figure 5). **5Ni-QD@HAP** showed the expected CH_4 conversion (ca. 45%) compared to **10Ni-QD@HAP**, but a significant low CO_2 conversion (10%). In addition, this catalyst showed a good stability (despite its limited activity) during 50 h of time-on-stream investigated (CH_4 and CO_2 conversions of 44% and 8% respectively after 50 h). A good CO selectivity (85-90%) but a moderate H_2 selectivity (*ca.* 58%) were achieved. The low hydrogen selectivity was probably related to the reverse water-gas shift reaction, in agreement with the low CO_2 conversion observed with this catalyst. The catalytic material prepared by impregnation (**5Ni@HAP_IWI**) showed almost the same initial methane conversion (42%) in comparison with **5Ni-QD@HAP** (45%). Nevertheless, this catalyst triggered a fast deactivation: CH_4 and CO_2 conversions quickly decreased from respectively 42 and 17% to 32 and 12% after 5 h of time-on-stream. The CO_2

conversion obtained with **5Ni@HAP_IWI** was slightly higher than that obtained with **5Ni-QD@HAP**, showing a low H_2 selectivity (50-55% after the deactivation step) and high CO selectivity (*ca.* 100%), due to the reverse water-gas-shift reaction.

5Ni@HAP exhibited an unexpected catalytic behavior. The CH_4 conversion continuously increased from the initial value of 35% up to 62% during the first 40 h, before stabilization was observed; CO_2 conversion continuously decreased from 48% to 14% in the initial 28 h on-stream before reaching stabilization around 20% up to the end of the reaction time studied (50 h). Taking into account the TPR profile of this catalyst showing its full reduction below 600 °C, we decided to carry out the TRM after pretreatment of **5Ni@HAP** by in-situ reduction at 800 °C for 2 h (instead of 700 °C), but no differences were observed (see Figure S17 in the Supporting Information). This behavior is in agreement with TPR profiles (Figure 2b), evidencing a complete reduction of nickel species below 600 °C. The reassembling of the active sites of the catalyst during the first 40 h of time-on-stream can explain the catalytic behavior observed. This fact may trigger the formation of single atom species of nickel on the catalyst surface (which could not be evidenced in this work), being less active in TRM reaction.[32]

Among the six catalysts evaluated in TRM, **10Ni@HAP** appeared to be the most efficient catalytic material. Thus, it was selected to perform an additional test at higher temperature (850 °C, see Table 2 and Figure S18 in the Supporting Information). No impact was observed for the methane conversion, reaching 91% conversion and being stable during 72 h of time-on-stream at both reaction temperatures (800 °C and 850 °C). Nevertheless, a decrease in the carbon dioxide conversion was observed at 850 °C. Since steam reforming is more influenced by the increase of temperature and methane conversion was not altered, the temperature increase probably favored the SMR against the DMR, justifying the lower CO_2 conversion at 850 °C than 800 °C.[45] Moreover, above 700 °C, the water-gas shift reaction is more favorable, consuming water and generating hydrogen and carbon dioxide. These results are consistent with the work reported by

Abreu *et al.*, who studied the kinetics of TRM reaction using Ni/γ-Al_2O_3 without observing any difference between methane conversion at 800 and 850 °C and a decrease in carbon dioxide conversion.[46] Moreover, Walker *et al.* reported that an increase in steam conversion usually leads to a decrease of CO_2 conversion in TRM.[47]

Regarding the activity, the highest total turnover frequency values (TTOF, see Supporting Information for its calculation) were obtained for the catalytic materials prepared by the organometallic approach featuring small NiNPs, enabled higher TTOF (up to ca. 420 h^{-1}) than the counterparts prepared by IWI (up to ca. 320 h^{-1}), constituted of large and non-uniformly distributed Ni particles on the support, being **10Ni@HAP** the most performant catalyst (see Figure S19 in the Supporting Information).

Table 2. Performance of catalytic materials at 10 wt.% and 5 wt.% Ni loading towards TRM.[a]

	Conversion (%)		Selectivity		Stability[b]
	CH_4	CO_2	H_2	CO	
10Ni@HAP	92	61	87	87	72 h
10Ni-QD@HAP	89	52	83	83	72 h
10Ni/HAP_IWI	78-72	71-30	92	100	52 h
5Ni@HAP	35-62	48-14	35-75	99-79	52 h (with pre-activation up to 40 h)
5Ni-QD@HAP	45-44	10-8	58	85-90	40 h
5Ni/HAP_IWI	42-17	32-12	50-55	100	5 h

[a] Conditions: 800 °C, 1.4 bar (total pressure), $CH_4/CO_2/H_2O/O_2$ = 63.3:30.7:0.04:5.95 molar fraction, GHSV = 14.9 $L \cdot gcat^{-1} \cdot h^{-1}$. [b] Reactions up to 72 h time-on-stream.

The catalytic materials mixed with alumina were characterized by TGA in air after TRM (see Figure S20 in the Supporting Information). The first mass loss centered around 80 °C could

be related to the removal of CO_2 and H_2O physisorbed on the catalytic materials.[48] For **10Ni-QD@HAP** and **5Ni-QD@HAP**, both C_α (peak at 30-120 °C) and C_β (peak at 450-675 °C), which are highly oriented carbon species responsible of catalyst deactivation by coke deposition,[49] were observed, with important mass loss of 5-7% due to the total oxidation of these carbon species under TGA conditions. Contrarily, for the catalytic materials prepared by the organometallic approach in the absence of QD (**10Ni@HAP** and **5Ni@HAP**), only C_α was present at low content. This fact indicates that the organic ligand was concomitantly decomposed during TRM, leading to C_β. A small mass gain was also observed for the used **10Ni@HAP** and **5Ni@HAP**, as evidenced by the DTG curves, which can be attributed to the oxidation of metallic nickel during TGA analysis. For the catalytic materials prepared by impregnation, **5Ni@HAP_IWI** and **10Ni@HAP_IWI**, both C_α and C_β were observed, explaining their fast deactivation. These results showed that the catalysts containing NiNPs smaller than 5 nm (catalytic materials prepared by the organometallic approach) lead to better catalytic performance than the catalytic materials featuring large particles and agglomerates obtained by the conventional impregnation method.

The presence of a high amount of alumina in comparison with that of nickel hampered the observation by TEM analysis if small Ni NPs remained in the catalytic material after TRM at 800 ºC (see Figure S21 in the Supporting Information). However, the formation of structured carbons (whisker and nanotube shapes) as well as big nickel nanoparticles (from 15 to 35 nm) were observed in contrast to the small nanoparticles size for fresh catalysts prepared by the organometallic strategy (<5 nm) (see Figure S22 in the Supporting Information).

To sum up, four different HAP-supported nickel catalysts with and without stabilizer at 5 and 10 wt.% Ni loadings were prepared featuring nickel NPs below 5 nm, which were then fully characterized and evaluated in TRM. The organometallic methodology employed herein enabled the preparation of catalytic materials precluding the replacement of Ca(II) by Ni(II) on HAP which is otherwise unavoidable using conventional incipient wetness impregnation techniques

and ultimately diminishes the stability of the catalysts. Most notably, the as-prepared materials showed higher MSI interactions and specific surface areas than the ones prepared by the conventional incipient wetness impregnation method.

In particular, catalysts obtained via the organometallic decomposition approach at 10 and 5 wt.% catalyst loadings featuring spherical nanoparticles of mean diameters in the range of 3.8 – 4.4 nm, and 2.6 – 2.8 nm, respectively, with dispersions up to 8 to 14 times higher than the ones obtained by incipient wetness impregnation, yielded also higher catalytic performances in TRM under the operating conditions at 800-850 ºC, 1.4 bar and up to 14.9 $L \cdot g_{cat}^{-1} \cdot h^{-1}$ GHSV. In addition, TPR analysis of the as-prepared catalytic materials revealed distinct reducibility patterns between materials prepared by incipient impregnation and the organometallic decomposition method which allowed to assess the nickel-support interactions via the evaluating of the resiliency of different types of Ni−O bonds towards reduction. In particular, materials prepared via incipient impregnation showed only high intensity TPR peaks in the range of 381-411 °C characteristic for the reduction of NiO species weakly interacting with the support.[33] On the contrary, all four materials prepared by the organometallic decomposition approach presented distinctive TPR peaks at higher temperatures, which attest the formation of Ni−O interactions with the support; thus, requiring hasher reduction conditions. In particular, the peaks appearing between 485-587 °C, diagnostic for the reduction of *β*-type NiO species have been observed for all four materials **10Ni@HAP**, **10Ni-QD@HAP**, **5Ni-QD@HAP and 5Ni-QD@HAP**.[35] Thus, these results indicate the key influences in terms of stronger metal support interactions and higher surface area observed for the latter towards the enhancement of catalytic performance. Overall, **10Ni@HAP** and **10Ni-QD@HAP** exhibited the best results towards TRM in terms of catalyst efficiency with methane conversions between 89-92%, good stability during long reaction time (up to 72 h), and high hydrogen and carbon monoxide selectivities (80-90%). The results of this work contribute to the development of robust catalysts for TRM reaction with enhanced reactivity and selectivity profiles for future industrial implementation of energy efficient processes integrating the

synergistic combination of the exothermic oxidation of methane to leverage endothermic dry reforming and steam reforming of methane.

ASSOCIATED CONTENT

Supporting Information. General instrumentation, experimental procedures and materials used; optimization of reaction parameters for the synthesis of supported Ni nanoparticles on hydroxyapatite and characterization of the as-prepared catalyst(s); determination of conversion, selectivity and dispersion; Figures S1-S22; Schemes S1-S4; and Tables S1-S4.

AUTHOR INFORMATION

Corresponding Authors

Doan Pham Minh - *Université de Toulouse, IMT Mines Albi, UMR CNRS 5302, Centre RAPSODEE, Campus Jarlard, 81013 Albi Cedex 9 (France).* https://orcid.org/0000-0001-7770-1487. *Email: doan.phamminh@mines-albi.fr

Daniel Pla - *Laboratoire Hétérochimie Fondamentale et Appliquée, UMR CNRS 5069, Université Toulouse 3 – Paul Sabatier, 118 route de Narbonne, 31062 Toulouse Cedex 9 (France)*. https://orcid.org/0000-0002-8703-8778. *Email: pla@lhfa.fr

Montserrat Gómez - *Laboratoire Hétérochimie Fondamentale et Appliquée, UMR CNRS 5069, Université Toulouse 3 – Paul Sabatier, 118 route de Narbonne, 31062 Toulouse Cedex 9 (France)*. https://orcid.org/0000-0003-1211-1333. * Email: montserrat.gomez-simon@univ-tlse3.fr

Authors

Alejandro Pérez Alonso - *Laboratoire Hétérochimie Fondamentale et Appliquée, UMR CNRS 5069, Université Toulouse 3 – Paul Sabatier, 118 route de Narbonne, 31062 Toulouse Cedex 9 (France).* https://orcid.org/0000-0002-0768-0219.

Alejandro Serrano-Maldonado - *Laboratoire Hétérochimie Fondamentale et Appliquée, UMR CNRS 5069, Université Toulouse 3 – Paul Sabatier, 118 route de Narbonne, 31062 Toulouse Cedex 9 (France).* https://orcid.org/0000-0003-3076-854X.

Jean-Bernard Ledeuil - *Université de Pau et des Pays de l'Adour, E2S UPPA, CNRS, IPREM, Pau (France).* https://orcid.org/0000-0002-7366-2190.

Lénaïc Madec - *Université de Pau et des Pays de l'Adour, E2S UPPA, CNRS, IPREM, Pau (France).* https://orcid.org/0000-0002-7681-1681

Notes

The authors declare no competing financial interest.

ACKNOWLEDGMENTS

The Centre National de la Recherche Scientifique (CNRS), IMT Mines Albi and the Université Toulouse 3-Paul Sabatier are gratefully acknowledged for their financial support. Authors thank POCTEFA Interreg program for funding (EFA308/19 TRIPyr) and EUR BIOECO in the framework of the "Investissements d'Avenir" program (ANR-18-EURE-0021). A. P. A. thanks the Université Fédérale de Toulouse for his doctoral fellowship (APR2019-CATPROC). The authors also acknowledge S. Mallet-Ladeira and C. Pradel for their helpful discussions on PXRD and (HR)TEM analyses, respectively.

REFERENCES

(1) Pham, T. T. P.; Ro, K. S.; Chen, L.; Mahajan, D.; Siang, T. J.; Ashik, U. P. M.; Hayashi, J.-i.; Pham Minh, D.; Vo, D.-V. N. Microwave-assisted dry reforming of methane for syngas production: a review. *Environ. Chem. Lett.* **2020**, *18*, 1987-2019, https://doi.org/10.1007/s10311-020-01055-0.

(2) Aramouni, N. A. K.; Touma, J. G.; Tarboush, B. A.; Zeaiter, J.; Ahmad, M. N. Catalyst design for dry reforming of methane: Analysis review. *Renew. Sust. Energ. Rev.* **2018**, *82*, 2570-2585, https://doi.org/10.1016/j.rser.2017.09.076.

(3) Komada, H.; Obata, K.; Li, D.; Sarathy, S. M.; Takanabe, K. Consequence of products from oxidative coupling of methane in a non-oxidative high temperature environment. *Catal. Sci. Technol.* **2023**, *13*, 2142-2150, https://doi.org/10.1039/D2CY02145E.

(4) Alsudani, F. T.; Saeed, A. N.; Ali, N. S.; Majdi, H. S.; Salih, H. G.; Albayati, T. M.; Saady, N. M. C.; Shakor, Z. M. Fisher-Tropsch Synthesis for Conversion of Methane into Liquid Hydrocarbons through Gas-to-Liquids (GTL) Process: A Review. *Methane* **2023**, *2*, 24-43, https://doi.org/10.3390/methane2010002.

(5) Wu, X.; Lang, J.; Jiang, Y.; Lin, Y.; Hu, Y. H. Thermo–Photo Catalysis for Methanol Synthesis from Syngas. *ACS Sustainable Chem. Eng.* **2019**, *7*, 19277-19285, https://doi.org/10.1021/acssuschemeng.9b05657.

(6) Li, D.; Yoshida, S.; Siritanaratkul, B.; Garcia-Esparza, A. T.; Sokaras, D.; Ogasawara, H.; Takanabe, K. Transient Potassium Peroxide Species in Highly Selective Oxidative Coupling of Methane over an Unmolten K_2WO_4/SiO_2 Catalyst Revealed by In

Situ Characterization. *ACS Catal.* **2021**, *11*, 14237-14248, https://doi.org/10.1021/acscatal.1c04206.

(7) Pham, X.-H.; Ashik, U.; Hayashi, J.-I.; Alonso, A. P.; Pla, D.; Gómez, M.; Pham Minh, D. Review on the catalytic tri-reforming of methane - Part II: Catalyst development. *Appl. Catal. A* **2021**, *623*, 118286, https://doi.org/10.1016/j.apcata.2021.118286.

(8) Pham Minh, D.; Pham, X.-H.; Siang, T. J.; Vo, D.-V. N. Review on the catalytic tri-reforming of methane-Part I: Impact of operating conditions, catalyst deactivation and regeneration. *Appl. Catal. A* **2021**, *621*, 118202, https://doi.org/10.1016/j.apcata.2021.118202.

(9) Lino, A. V. P.; Colmenares Calderon, Y. N.; Mastelaro, V. R.; Assaf, E. M.; Assaf, J. M. Syngas for Fischer-Tropsch synthesis by methane tri-reforming using nickel supported on $MgAl_2O_4$ promoted with Zr, Ce and Ce-Zr. *Appl. Surf. Sci.* **2019**, *481*, 747-760, https://doi.org/10.1016/j.apsusc.2019.03.140.

(10) Kang, J. S.; Kim, D. H.; Lee, S. D.; Hong, S. I.; Moon, D. J. Nickel-based tri-reforming catalyst for the production of synthesis gas. *Appl. Catal. A* **2007**, *332*, 153-158, https://doi.org/10.1016/j.apcata.2007.08.017.

(11) Majewski, A. J.; Wood, J. Tri-reforming of methane over Ni@SiO_2 catalyst. *Int. J. Hydrog. Energy* **2014**, *39*, 12578-12585, https://doi.org/10.1016/j.ijhydene.2014.06.071.

(12) Singha, R. K.; Shukla, A.; Yadav, A.; Adak, S.; Iqbal, Z.; Siddiqui, N.; Bal, R. Energy efficient methane tri-reforming for synthesis gas production over highly coke

resistant nanocrystalline Ni-ZrO_2 catalyst. *Appl. Energy* **2016**, *178*, 110-125, https://doi.org/10.1016/j.apenergy.2016.06.043.

(13) Singha, R. K.; Das, S.; Pandey, M.; Kumar, S.; Bal, R.; Bordoloi, A. Ni nanocluster on modified CeO_2-ZrO_2 nanoporous composite for tri-reforming of methane. *Catal. Sci. Technol.* **2016**, *6*, 7122-7136, https://doi.org/10.1039/C5CY01323B.

(14) Kozonoe, C. E.; Brito Alves, R. M.; Schmal, M. Influence of feed rate and testing variables for low-temperature tri-reforming of methane on the Ni@MWCNT/Ce catalyst. *Fuel* **2020**, *281*, 118749, https://doi.org/10.1016/j.fuel.2020.118749.

(15) Kumar, R.; Pant, K. K. Promotional effects of Cu and Zn in hydrotalcite-derived methane tri-reforming catalyst. *Appl. Surf. Sci.* **2020**, *515*, 146010, https://doi.org/10.1016/j.apsusc.2020.146010.

(16) Iablokov, V.; Beaumont, S. K.; Alayoglu, S.; Pushkarev, V. V.; Specht, C.; Gao, J.; Alivisatos, A. P.; Kruse, N.; Somorjai, G. A. Size-Controlled Model Co Nanoparticle Catalysts for CO_2 Hydrogenation: Synthesis, Characterization, and Catalytic Reactions. *Nano Lett.* **2012**, *12*, 3091-3096, https://doi.org/10.1021/nl300973b.

(17) Mamontova, E.; Favier, I.; Pla, D.; Gómez, M. Chapter Two - Organometallic interactions between metal nanoparticles and carbon-based molecules: A surface reactivity rationale. In *Adv. Organomet. Chem.*, Pérez, P. J. Ed.; Vol. 77; Academic Press 2022; pp 43-103. https://doi.org/10.1016/bs.adomc.2022.01.004.

(18) Reina, A.; Favier, I.; Pradel, C.; Gómez, M. Stable Zero-Valent Nickel Nanoparticles in Glycerol: Synthesis and Applications in Selective Hydrogenations. *Adv. Synth. Catal.* **2018**, *360*, 3544-3552, https://doi.org/10.1002/adsc.201800786.

(19) Mamontova, E.; Trabbia, C.; Favier, I.; Serrano-Maldonado, A.; Ledeuil, J.-B.; Madec, L.; Gómez, M.; Pla, D. Novel Catalyst Composites of Ni- and Co-Based Nanoparticles Supported on Inorganic Oxides for Fatty Acid Hydrogenations. *Nanomaterials* **2023**, *13*, 1435, https://doi.org/10.3390/nano13091435.

(20) Pérez Alonso, A.; Mauriés, S.; Ledeuil, J.-B.; Madec, L.; Pham Minh, D.; Pla, D.; Gómez, M. Nickel Nanoparticles Immobilized on Pristine Halloysite: An Outstanding Catalyst for Hydrogenation Processes. *ChemCatChem* **2022**, *14*, e2022007, https://doi.org/10.1002/cctc.202200775.

(21) Boukha, Z.; Gil-Calvo, M.; de Rivas, B.; Gonzalez-Velasco, J. R.; Gutierrez-Ortiz, J. I.; López-Fonseca, R. Behaviour of Rh supported on hydroxyapatite catalysts in partial oxidation and steam reforming of methane: on the role of the speciation of the Rh particles. *Appl. Catal. A* **2018**, *556*, 191-203, https://doi.org/10.1016/j.apcata.2018.03.002.

(22) Gonzalez Caranton, A. R.; Stavale, F.; Annese, E.; Gaioto, C.; Checca Huaman, N. R.; Assaf, J. M. Enhancing Catalytic Performance with Sol-Gel Hydrotalcite-Derived Nickel Oxide Catalysts for Dry Reforming of Methane: An Examination on Reactivity and Coke Formation. *ChemCatChem* **2023**, *15*, e202300280, https://doi.org/10.1002/cctc.202300280.

(23) Jun, J. H.; Lee, T.-J.; Lim, T. H.; Nam, S.-W.; Hong, S.-A.; Yoon, K. J. Nickel–calcium phosphate/hydroxyapatite catalysts for partial oxidation of methane to syngas: characterization and activation. *J. Catal.* **2004**, *221*, 178-190, https://doi.org/10.1016/j.jcat.2003.07.004.

(24) Leal-Duaso, A.; Favier, I.; Pla, D.; Pires, E.; Gómez, M. Design of Glycerol-Based Solvents for the Immobilization of Palladium Nanocatalysts: A Hydrogenation Study. *ACS Sustain. Chem. Eng.* **2021**, *9*, 6875-6885, https://doi.org/10.1021/acssuschemeng.1c01694.

(25) Serrano-Maldonado, A.; Bendounan, A.; Silly, M. G.; Pla, D.; Gómez, M. Selective catalytic hydrogenation of fatty acids with cobalt-halloysite nanocomposites for waste valorization. *ACS Appl. Nano Mater.* **2023**, *6*, 11317–11326, https://doi.org/10.1021/acsanm.3c01361.

(26) Thommes, M.; Kaneko, K.; Neimark, A. V.; Olivier, J. P.; Rodriguez-Reinoso, F.; Rouquerol, J.; Sing, K. S. Physisorption of gases, with special reference to the evaluation of surface area and pore size distribution (IUPAC Technical Report). *Pure Appl. Chem.* **2015**, *87*, 1051-1069, https://doi.org/10.1515/pac-2014-1117.

(27) Kang, Z.; Gao, H.; Hu, Z.; Jia, X.; Wen, D. Ni–Fe/Reduced Graphene Oxide Nanocomposites for Hexavalent Chromium Reduction in an Aqueous Environment. *ACS Omega* **2022**, *7*, 4041-4051, https://doi.org/10.1021/acsomega.1c05273.

(28) Rosario, A. V.; Pereira, E. C. The role of Pt addition on the photocatalytic activity of TiO_2 nanoparticles: The limit between doping and metallization. *Appl. Catal. B: Envir.* **2014**, *144*, 840-845, https://doi.org/10.1016/j.apcatb.2013.07.029.

(29) Katheria, S.; Gupta, A.; Deo, G.; Kunzru, D. Effect of calcination temperature on stability and activity of $Ni/MgAl_2O_4$ catalyst for steam reforming of methane at high pressure condition. *Int. J. Hydrog. Energy.* **2016**, *41*, 14123-14132, https://doi.org/10.1016/j.ijhydene.2016.05.109.

(30) Rabiei, M.; Palevicius, A.; Monshi, A.; Nasiri, S.; Vilkauskas, A.; Janusas, G. Comparing methods for calculating nano crystal size of natural hydroxyapatite using X-ray diffraction. *Nanomaterials* **2020**, *10*, 1627, https://doi.org/10.3390/nano10091627.

(31) Qiao, H.; Wei, Z.; Yang, H.; Zhu, L.; Yan, X. Preparation and Characterization of NiO Nanoparticles by Anodic Arc Plasma Method. *J. Nanomater.* **2009**, *2009*, 795928, https://doi.org/10.1155/2009/795928.

(32) Pham Minh, D. Introduction to Hydroxyapatite-based Materials in Heterogeneous Catalysis. In *Design and Applications of Hydroxyapatite-Based Catalysts*, Pham Minh, D. Ed.; 2022; pp 1-18. https://doi.org/10.1002/9783527830190.ch1.

(33) Boukha, Z.; Kacimi, M.; Pereira, M. F. R.; Faria, J. L.; Figueiredo, J. L.; Ziyad, M. Methane dry reforming on Ni loaded hydroxyapatite and fluoroapatite. *Appl. Catal. A* **2007**, *317*, 299-309, https://doi.org/10.1016/j.apcata.2006.10.029.

(34) Pedroarena, I.; Grande, L.; Torrez-Herera, J. J.; Korili, S. A.; Gil, A. Analysis by temperature-programmed reduction of the catalytic system Ni-Mo-Pd/Al_2O_3. *Fuel* **2023**, *334*, 126789, https://doi.org/10.1016/j.fuel.2022.126789.

(35) Rego de Vasconcelos, B.; Pham Minh, D.; Martins, E.; Germeau, A.; Sharrock, P.; Nzihou, A. Highly-efficient hydroxyapatite-supported nickel catalysts for dry reforming of methane. *Int. J. Hydrogen Energy* **2020**, *45*, 18502-18518, https://doi.org/10.1016/j.ijhydene.2019.08.068.

(36) Yaakob, Z.; Bshish, A.; Ebshish, A.; Tasirin, S. M.; Alhasan, F. H. Hydrogen production by steam reforming of ethanol over nickel catalysts supported on sol gel made

alumina: influence of calcination temperature on supports. *Materials* **2013**, *6*, 2229-2239, https://doi.org/10.3390/ma6062229.

(37) Yang, F.; Liu, D.; Zhao, Y.; Wang, H.; Han, J.; Ge, Q.; Zhu, X. Size Dependence of Vapor Phase Hydrodeoxygenation of m-Cresol on Ni/SiO_2 Catalysts. *ACS Catal.* **2018**, *8*, 1672-1682, https://doi.org/10.1021/acscatal.7b04097.

(38) Rego de Vasconcelos, B.; Minh, D. P.; Sharrock, P.; Nzihou, A. Regeneration study of Ni/hydroxyapatite spent catalyst from dry reforming. *Catal. Today* **2018**, *310*, 107-115, https://doi.org/10.1016/j.cattod.2017.05.092.

(39) Ho, C. R.; Defalque, V.; Zheng, S.; Bell, A. T. Propanol Amination over Supported Nickel Catalysts: Reaction Mechanism and Role of the Support. *ACS Catal.* **2019**, *9*, 2931-2939, https://doi.org/10.1021/acscatal.8b04612.

(40) Boukha, Z.; Yeste, M. P.; Cauqui, M. Á.; González-Velasco, J. R. Influence of Ca/P ratio on the catalytic performance of Ni/hydroxyapatite samples in dry reforming of methane. *Appl. Catal. A* **2019**, *580*, 34-45, https://doi.org/10.1016/j.apcata.2019.04.034.

(41) Mirghni, A. A.; Madito, M. J.; Oyedotun, K. O.; Masikhwa, T. M.; Ndiaye, N. M.; Ray, S. J.; Manyala, N. A high energy density asymmetric supercapacitor utilizing a nickel phosphate/graphene foam composite as the cathode and carbonized iron cations adsorbed onto polyaniline as the anode. *RSC Adv.* **2018**, *8*, 11608-11621, https://doi.org/10.1039/C7RA12028A.

(42) Pérez Alonso, A.; Pham Minh, D.; Pla, D.; Gómez, M. A Cooperative Rh/Co-Catalyzed Hydroaminomethylation Reaction for the Synthesis of Terpene Amines. *ChemCatChem* **2023**, *15*, e202300501, https://doi.org/10.1002/cctc.202300501.

(43) Chiodini, A.; Bua, L.; Carnelli, L.; Zwart, R.; Vreugdenhil, B.; Vocciante, M. Enhancements in Biomass-to-Liquid processes: Gasification aiming at high hydrogen/carbon monoxide ratios for direct Fischer-Tropsch synthesis applications. *Biomass Bioenerg.* **2017**, *106*, 104-114, https://doi.org/10.1016/j.biombioe.2017.08.022.

(44) Wei, W.; Jinlong, G. Methanation of carbon dioxide: an overview. *Front. Chem. Sci. Eng.* **2011**, *5*, 2-10, https://doi.org/10.1007/s11705-010-0528-3.

(45) Chein, R.; Chen, Y.; Yu, C.; Chung, J. Thermodynamic analysis of dry reforming of CH_4 with CO_2 at high pressures. *J. Nat. Gas Sci. Eng.* **2015**, *26*, 617-629, https://doi.org/10.1016/j.jngse.2015.07.001.

(46) Maciel, L.; de Souza, A.; Cavalcanti-Filho, V.; Knoechelmann, A.; de Abreu, C. Kinetic evaluation of the tri-reforming process of methane for syngas production. *React. Kinet. Mech. Catal.* **2010**, *101*, 407-416, https://doi.org/10.1007/s11144-010-0232-9.

(47) Walker, D. M.; Pettit, S. L.; Wolan, J. T.; Kuhn, J. N. Synthesis gas production to desired hydrogen to carbon monoxide ratios by tri-reforming of methane using Ni–MgO–(Ce, Zr)O_2 catalysts. *Appl. Catal. A* **2012**, *445*, 61-68, https://doi.org/10.1016/j.apcata.2012.08.015.

(48) Özdemir, H.; Öksüzömer, M. F.; Gürkaynak, M. A. Preparation and characterization of Ni based catalysts for the catalytic partial oxidation of methane: Effect of support basicity on H_2/CO ratio and carbon deposition. *Int. J. Hydrog. Energy* **2010**, *35*, 12147-12160, https://doi.org/10.1016/j.ijhydene.2010.08.091.

(49) Özdemir, H.; Öksüzömer, M. F.; Gürkaynak, M. A. Effect of the calcination temperature on Ni/$MgAl_2O_4$ catalyst structure and catalytic properties for partial oxidation of methane. *Fuel* **2014**, *116*, 63-70, https://doi.org/10.1016/j.fuel.2013.07.095.

Pérez Alonso, A.; Serrano-Maldonado, A.; Ledeuil, J.-B.; Madec, L.; Minh, D. P.; Pla, D.; Gómez, M. Advanced Nickel-based Catalytic Materials on Hydroxyapatite: Effect of the Metal Particle Size on Tri-reforming of Methane. *ACS Sustainable Resour. Manage.* **2024**, https://doi.org/10.1021/acssusresmgt.3c00099

FOR TABLE OF CONTENTS USE ONLY

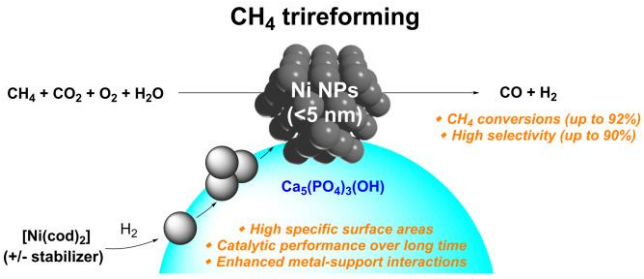

Small and well-dispersed nickel nanoparticles immobilized on hydroxyapatite led to efficient and highly selective methane tri-reforming catalysts enabling the production of syngas via the valorization of green-house gases.

KEYWORDS

Ni-based catalytic materials, Hydroxyapatite, Trireforming of methane, Greenhouse gases, Syngas feedstock

SYNOPSIS

The innovative design of nickel-based catalytic materials enabled the simultaneous conversion of CH_4 and CO_2 into syngas feedstock, representing a new paradigm for green-house gas abatement.